Journal of Energy Storage 124 (2025) 116438

Contents lists available at ScienceDirect

Journal of Energy Storage

journal homepage: www.elsevier.com/locate/est

Research papers

Cascaded electrochemical-thermal modeling and temperature estimation for cylindrical Li-ion batteries

Patryck Ferreira, Shu-Xia Tang *

Department of Mechanical Engineering, Texas Tech University, Lubbock, 79409, TX, USA

ARTICLE INFO

Keywords:
Lithium-ion batteries
Thermal modeling
Sensor placement
Electrochemical model
Temperature estimation

ABSTRACT

Cascaded electrochemical-thermal modeling is essential for understanding the intricate temperature dynamics of lithium-ion batteries, which directly impact their safety, performance, and longevity. This study introduces a comprehensive multi-layer model that captures detailed thermal and electrochemical interactions across all layers and components of a cylindrical lithium-ion battery. While the multi-layer model provides precise temperature distribution and might identify potential hotspots, its complexity makes real-time applications challenging. To address this, a simplified single-layer model is developed, focusing on a single representative layer with eight components. This model reduces computational demands, enabling efficient real-time temperature estimation. Experimental validation demonstrates the superior accuracy of the multi-layer model compared to the single-layer model, which trades detail for simplicity. To bridge the gap between accuracy and practicality, an optimized sensor placement strategy is proposed, supported by a Luenberger observer to estimate battery case temperatures using experimental data. These findings underscore the potential of the proposed models to enhance thermal safety, optimize monitoring, and guide the development of next-generation battery technologies.

1. Introduction

Li-ion batteries (LiBs) have been essential for advancing sustainable energy solutions since their commercialization by Sony in the 1990s [1]. Renowned for their high energy density, long cycle life, and low self-discharge rates, LiBs have become the power source of choice for a wide range of applications, from simple watches and consumer electronics to electric vehicles (EVs) and renewable energy storage systems [2]. These attributes distinguish LiBs from other rechargeable battery technologies, such as nickel-cadmium (NiCd) and nickel-metal hydride (NiMH), making them indispensable in modern energy storage and utilization [3].

LiBs operate by moving lithium ions between the anode and cathode during charging and discharging. The materials used in these components directly impact battery performance. Early LiBs utilized $LiCoO_2$ cathodes [4], but newer materials like $LiFePO_4$, LMO, and NMC offer enhanced stability and longer cycle life [5,6]. For instance, $LiFePO_4$ provides superior thermal stability and durability, making it suitable for large-scale applications such as EVs and renewable energy systems [7].

Despite these advancements, thermal management remains a significant challenge. As the energy density of LiBs increases, heat generation during operation also rises due to higher electrochemical activity, necessitating effective cooling systems to ensure safety and maintain performance [8]. Poor heat dissipation can result in uneven cell temperatures, leading to overheating, capacity loss, and, in severe cases, thermal runaway [9].

Thermal runaway is a critical safety risk in high-power LiB applications, particularly in EVs and grid storage systems. This makes accurate thermal modeling essential for preventing overheating and enhancing safety [10,11]. However, many electrochemical-thermal models rely on simplifications that fail to capture detailed internal temperature distributions, limiting their ability to predict localized heating and thermal imbalances.

Although electrochemical-thermal modeling has significantly evolved, a large number of models still overlook internal temperature gradients, especially under dynamic, high-power conditions. Low-order models typically estimate core or surface temperatures [12], which can diverge from actual internal values, resulting in thermal prediction inaccuracies. High-fidelity models improve accuracy but are often computationally intensive, limiting their use in real-time applications [13]. These models generally rely on solvers like COMSOL [14–16] and ANSYS [17,18] to handle the coupled electrochemical-thermal equations.

To strike a balance between accuracy and efficiency, recent studies have introduced reduced-order models capable of estimating internal

* Corresponding author.
E-mail address: shuxia.tang@ttu.edu (S.-X. Tang).

https://doi.org/10.1016/j.est.2025.116438
Received 22 January 2025; Received in revised form 21 March 2025; Accepted 25 March 2025
2352-152X/© 2025 Elsevier Ltd. All rights are reserved, including those for text and data mining, AI training, and similar technologies.

temperature distributions with significantly lower computational costs. These models are widely applied in thermal state monitoring and Battery Management Systems (BMS) [19,20]. For instance, a reduced-order thermal model for liquid-cooled battery packs has demonstrated the ability to capture transient thermal dynamics efficiently [21]. Despite these benefits, many reduced-order models still lack the resolution needed to capture localized heating effects critical for predicting thermal runaway and optimizing thermal management.

Refinements to reduced-order modeling have introduced core-surface frameworks that divide the battery into distinct thermal zones connected by thermal resistance [22,23]. Impedance-based approaches and extended Kalman filters have enabled estimation of 2D temperature fields in cylindrical cells [24], and dual unscented Kalman filters have been proposed to simultaneously estimate core temperature and State-of-Charge (SoC), enhancing robustness under varying loads [25]. Coupled PDE-ODE frameworks have further improved SoC and thermal predictions [26], alongside adaptive observers for online parameter identification [27].

Thermal models for cells, such as in [28], assume uniform heat generation. More recent works have scaled these models to the pack level to support uniform temperature distribution across large battery systems [29]. Yet, many still face limitations in real-time applications due to computational complexity or oversimplification particularly in high-power systems where rapid thermal transients may result in undetected hotspots.

In a preliminary study [30], electrolyte dynamics were modeled solely in the negative electrode. However, experimental disassembly revealed that the electrolyte interacts with all internal components, highlighting the need for a more detailed framework. Incorporating these interactions improves the accuracy of temperature predictions and internal heat generation dynamics.

To address these challenges, this study proposes both multi-layer and single-layer electrochemical-thermal models that aim to enhance thermal accuracy while remaining computationally efficient. The main contributions include:

- **Development and validation of a comprehensive multi-layer model** that captures detailed internal temperature distributions and resolves thermal gradients critical to safety and performance.
- **Implementation of a simplified single-layer model** that retains essential thermal dynamics with lower computational burden, suitable for real-time BMS integration.
- **Integration of electrochemical and thermal dynamics** to model heat generation, dissipation, and their interactions, improving physical fidelity.
- **Experimental validation** demonstrating strong alignment between model simulations and measured thermal behavior.
- **Proposal of a sensor placement strategy and use of a Luenberger observer** to estimate battery case temperature, enabling real-time thermal monitoring and management.

The article is organized as follows: Section 2 introduces the electrochemical-thermal model. Within this section, the cylindrical battery is disassembled, and its structure is discussed as the foundation for the model, considering practical constraints. Electrochemical heat generation and modeling are detailed in Section 2.3. Sensor placement and temperature estimation are discussed in Section 3. Section 4 presents the experimental validation and discussion. Finally, Section 5 provides conclusions and outlines directions for future work.

To ensure consistency and clarity, Table 1 provides a comprehensive list of symbols and parameters used throughout this paper.

Table 1
List of Symbols and Parameters.

Symbol	Definition	Unit
Q_i	Heat generation at component i	W
$q_{\text{cond},i}$	Heat by conduction at component i	W
$q_{\text{conv},i}$	Heat by convection at component i	W
T_i	Temperature at component i	K
S	Electrochemical heat generation	W
V	Voltage	V
I	Current	A
$j^{\pm}$	Molar flux	mol/(m^2·s)
$c_{ss}^{\pm}$	Surface lithium-ion concentration	mol/m^3
$c_{\text{e},0}$	Initial electrolyte concentration	mol/m^3
$\dot{E}_{\text{st},i}$	Stored energy rate at component i	W
$\dot{E}_{\text{g},i}$	Generated energy rate at component i	W
$\dot{E}_{\text{in},i}$	Energy inflow at component i	W
$\dot{E}_{\text{out},i}$	Energy outflow at component i	W
Parameters		
ρ_i	Density of component i	kg/m^3
$c_{\text{p},i}$	Specific heat capacity of component i	J/(kg ·K)
D_{i}	Initial layer diameter	m
D_{e}	Case diameter	m
$D_{s^{\pm}}$	Diffusion coefficient of electrodes	m^2/s
H	Battery height	m
k_i	Thermal conductivity of component i	W/(m ·K)
L_i	Thickness of component i	m
R_i	Thermal resistance of component i	K/W
R_{air}	Thermal resistance to ambient air	K/W
v_i	Volume of component i	m^3
h	Convective heat transfer coefficient	W/(m^2 ·K)
$\phi_s^{\pm}$	Solid-phase potentials	V
$\eta^{\pm}$	Overpotential	V
$U^{\pm}$	Equilibrium potential	V
$a_s^{\pm}$	Interfacial surface area	m^2
α	Charge transfer coefficient	–
$i_0^{\pm}$	Exchange current density	A/m^2
R	Universal gas constant	J/(mol ·K)
F	Faraday constant	C/mol
Subscripts		
0	Electrolyte	–
2,4	Negative electrode	–
6,8	Positive electrode	–
1,5	Separator	–
7	Positive current collector	–
3	Negative current collector	–
9	Case	–

2. Electrochemical-thermal model

This section introduces the thermal and electrochemical model of the LiBs. The integrated approach captures the interaction between electrochemical processes and thermal effects within the battery structure, offering a comprehensive understanding of heat generation, temperature distribution, and their influence on battery performance. The relationship between electrochemical and thermal processes follows a cascaded structure: the voltage derived from electrochemical reactions serves as the input for calculating electrochemical heat, which in turn links the electrochemical and thermal domains. These concepts will be explored in detail in the following subsections.

2.1. Cylindrical Lithium-ion battery structure

Fig. 1(a) illustrates the internal structure of a LiB, highlighting its tightly wound layers, which are designed to maximize surface area for efficient electrochemical reactions. A detailed disassembly of the LiB at the Distributed Parameter Systems & Control Lab confirmed the component sequence: separator (gray), negative electrode (blue), positive electrode (pink), and collectors (black and red), comprising a total of 38 layers.

Unlike the commonly assumed 6-component structure, which is typically associated with pouch and coin cells [31,32], each layer in the model consists of 8 components due to the observed structure, in which an additional negative electrode and positive electrode are included within each repeating sequence. Specifically, each layer consists of: separator, negative electrode, negative collector, negative electrode

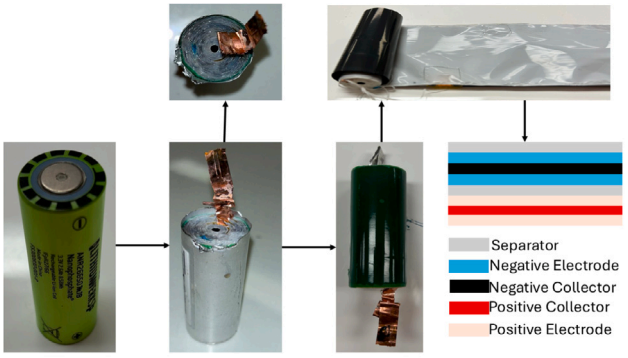

(a) Structure of a cylindrical battery.

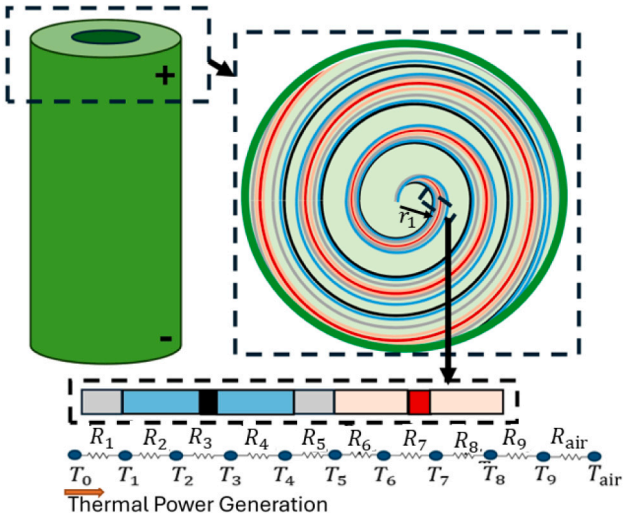

(b) Schematic of the spiral-wound structure and the thermal power generation model for each internal component. The colors of the components follow the legend in Fig. 1(a).

Fig. 1. Comparison between the real structure of a cylindrical battery and its schematic representation.

(again), separator, positive electrode, positive collector, and positive electrode (again). This structure was verified through battery disassembly, ensuring that the model accurately represents the physical arrangement of components in the studied cell. The number of layers aligns with the findings in [33] for a 26650 cell.

The thermal model developed in this study improves temperature distribution accuracy by incorporating electrolyte interactions with all internal components, leading to a more realistic heat transfer representation. Unlike the approach in [30], where electrolyte dynamics were modeled only for the negative electrode as part of a preliminary model, our approach accounts for interactions across the entire structure, capturing internal heat generation and dissipation more effectively. Additionally, battery disassembly in this study revealed differences in the component sequence compared to the configuration described in [30], which followed the arrangement proposed in [34], starting with the negative collector and progressing toward the negative electrode. However, our experimental analysis Fig. 1(a) indicates that this sequence does not fully represent the actual battery structure observed in our case, where the arrangement begins with the separator.

The thermal model schematic Fig. 1(b) represents the temperature distribution using the thermal resistances of each component. It incorporates key parameters, including the electrolyte temperature (T_0), negative collector temperature and resistance (T_3, R_3), positive collector temperature and resistance (T_7, R_7), separator temperatures and resistances (T_1, T_5, R_1, R_5), negative electrode temperatures and resistances (T_2, T_4, R_2, R_4), positive electrode temperatures and resistances (T_6, T_8, R_6, R_8), case temperature and resistance (T_9, R_9), and ambient conditions (T_{air}, R_{air}). Heat is assumed to be generated at the center of the battery due to electrochemical reactions, conducted between components, and convected between the electrolyte and the internal components. It is dissipated radially through each layer along resistive and thermal paths.

2.2. Thermal model

The thermal model adheres to the principle of energy conservation and is described as follows:

$$\dot{E}_{\mathrm{st},i}(t,r,\theta,z) = \dot{E}_{\mathrm{in},i}(t,r,\theta,z) - \dot{E}_{\mathrm{out},i}(t,r,\theta,z) + \dot{E}_{\mathrm{g},i}(t,r,\theta,z), \tag{1}$$

for $i \in \overline{0,9} = \{0,1,2,3,4,5,6,7,8,9\}$, $(r,\theta,z) \in \mathbb{R}^3$ are cylindrical coordinates. Here, $\dot{E}_{\mathrm{st},i}$ denotes the rate of energy stored in the material, $\dot{E}_{\mathrm{in},i}$ is the rate of energy entering the components, $\dot{E}_{\mathrm{out},i}$ is the rate of energy exiting the components, and $\dot{E}_{\mathrm{g},i}$ represents the rate of thermal power generated within the components.

The cylindrical battery model assumes distinct thermal behaviors along the radial (r) and axial (z) directions due to internal arrangement and material properties. Heat conduction is generally more efficient along the z-direction, resulting in a more uniform temperature profile along the battery's length compared to the radial direction. This behavior is reinforced by the assumption of adiabatic conditions at the battery's ends, where heat exchange is negligible due to limited convection. This assumption is commonly used in battery thermal modeling, particularly for naturally or air-cooled battery systems. Prior studies [12] indicate that, due to the internal battery arrangement, heat conduction along the z-direction is more effective, resulting in a more uniform temperature profile. Furthermore, experimental validation from [12] confirms that under natural convection cooling conditions, surface-convection heat transfer at the battery ends is negligible. These findings support the assumption of limited axial heat dissipation in the present model.

Consequently, the terms $\dot{E}_{\mathrm{in},i}$ and $\dot{E}_{\mathrm{out},i}$ in Eq. (1) become zero for $i \in \overline{0,9}$, simplifying Eq. (1) to:

$$\dot{E}_{\mathrm{st},i}(t) = \dot{E}_{\mathrm{g},i}(t). \tag{2}$$

The stored energy rate and generated heat are defined as [35, Chapter 2, Section 2.3]:

$$\dot{T}_i(t) = \frac{Q_i(t)}{\rho_i c_{\mathrm{p},i}}, \tag{3}$$

where ρ_i is the density, $c_{\mathrm{p},i}$ is the heat capacity, and $Q_i(t)$ represents heat generation:

$$Q_i(t) = \frac{S(t)}{\sum_{\substack{j=0 \\ j\neq i}}^{8} v_j} + \frac{q_{\mathrm{cond},i}(t)}{v_i} + \frac{q_{\mathrm{conv},i}(t)}{v_i}, \tag{4}$$

where v_i is the volume of each component. Here, $q_{\mathrm{cond},i}$ is heat due to conduction between components, $q_{\mathrm{conv},i}$ is heat due to convection between the liquid electrolyte and internal components, and $S(t)$ denotes electrochemical heat. The volume v_j excludes the case.

The heat conduction equation is:

$$q_{\mathrm{cond},i}(t) = \frac{\Delta T_i(t)}{R_i}, \tag{5}$$

for $i \in \overline{0,9}$, where $\Delta T_i(t)$ denotes the temperature difference between interacting components, and R_i represents the thermal resistance between these components. Since the electrolyte is liquid, its thermal conductivity is significantly lower than that of the solid components, and its contribution to heat conduction is often negligible in thermal modeling [36,37]. Therefore, in this work, $q_{\mathrm{cond},0} = 0$, resulting in the absence of thermal resistance R_0 in the electrolyte.

The calculation order of $\Delta T_i(t)$ should follow the sequence of resistances shown in Fig. 1(b). The thermal resistance for each battery layer is given by:

$$R_i = \frac{1}{2\pi k_i L_i} \ln\left(\frac{r_2}{r_1}\right), \tag{6}$$

where k_i is thermal conductivity, L_i is the layer length, and r_1 and r_2 are the inner and outer radii of each layer.

Newton's cooling law is used to describe convection and is expressed as follows:

$$q_{\text{conv},i}(t) = hA\Delta T_i(t), \tag{7}$$

where h represents the electrolyte's convective heat transfer coefficient, A is the electrolyte's area, and $\Delta T_i(t)$ is the temperature difference between the electrolyte and each internal component in contact with it. The convection between the electrolyte and the case is zero.

2.2.1. The temperature dynamics of the battery components

For the electrolyte dynamics, the conduction term $q_{\text{cond},0} = 0$ is zero. Thus, only convection in the liquid electrolyte and heat due to electrochemical reactions remain. Therefore, the equation for the electrolyte dynamics is given by:

$$\begin{aligned}\dot{T}_0(t) = {} & \frac{S(t)}{\rho_0 c_{\text{p}0} \sum_{\substack{j=0\\ j\neq i}}^{8} v_j} + \frac{hA}{\rho_0 c_{\text{p}0} v_0}\Big[(T_0(t) - T_1(t))\Big] + \frac{hA_1}{\rho_0 c_{\text{p}} v_0}\Big[(T_0(t) - T_2(t)) \\ & + (T_0(t) - T_3(t)) + (T_0(t) - T_4(t)) + (T_0(t) - T_5(t)) + (T_0(t) - T_6(t)) \\ & + (T_0(t) - T_7(t)) + (T_0(t) - T_8(t))\Big],\end{aligned} \tag{8}$$

where v_0 represents the volume of the electrolyte in the battery, ρ_0 denotes the density of the electrolyte, and $c_{\text{p}0}$ is the heat capacity of the electrolyte. Here, A represents the area corresponding to r_1, as shown in Fig. 1(b), while A_1 represents the area between the internal components.

In the solid components of the battery, heat is transferred by conduction between these components, convection with the liquid electrolyte, and additional heat generation from electrochemical reactions. The temperature dynamics for each solid component follows the same pattern and is given by:

$$\dot{T}_{8(k-1)+i}(t) = \frac{S(t)}{\rho_i c_{\text{p},i} \sum_{\substack{j=1\\ j\neq i}}^{8} v_j} + \frac{\Delta T_{k,i}(t)}{v_i \rho_i c_{\text{p},i} R_i} - \frac{hA(T_0(t) - T_{k,i}(t))}{v_i \rho_i c_{\text{p},i}}, \tag{9}$$

$$\Delta T_{k,i}(t) = \begin{cases} T_{k-1,8}(t) - T_{k,1}(t), & \text{if } i = 1 \text{ and } k > 1 \\ T_{k,i-1}(t) - T_{k,i}(t), & \text{otherwise,} \end{cases} \tag{10}$$

where v_i denotes the volume, ρ_i its density, and $c_{\text{p},i}$ its heat capacity. k denotes the layer index and i represents the component index, with $k \in \overline{1,38}$, and $i \in \overline{1,8}$.

For the battery casing, the temperature equation is formulated as follows:

$$\dot{T}_{305}(t) = \frac{T_{\text{air}}(t) - T_{305}(t)}{v_9 \rho_9 c_{\text{p}9} R_{\text{air}}} - \frac{T_{305}(t) - T_{304}(t)}{v_9 \rho_9 c_{\text{p}9} R_9}, \tag{11}$$

where v_9, ρ_9, $c_{\text{p}9}$, R_9, and R_{air} denote the volume, density, heat capacity, thermal resistance of the case, and thermal resistance of the air, respectively. External thermal interactions, such as cooling and insulation, are incorporated into the model through the thermal resistances of the casing and air (R_9 and R_{air}). Note that index 305 corresponds to the component labeled as 9 in Fig. 1(b). By adjusting these parameters, different cooling conditions (e.g., forced convection, natural convection) and insulation effects can be accounted for without modifying the governing equation. Since the casing does not participate in electrochemical reactions, there is no internal electrochemical heat generation in this region, justifying the assumption that $S(t) = 0$ at the surface. Furthermore, studies such as [15,38,39] support the assumption that heat generation occurs exclusively within the internal components of the battery.

2.2.2. Multi-layer model

A complex and detailed model, known as the multi-layer model, is derived from the preceding equations. This model accounts for each layer within the cylindrical battery, providing a comprehensive analysis of temperature distribution and reaction dynamics across the layers. It captures layer-specific thermal and electrochemical interactions, making it particularly valuable for examining internal temperature gradients especially in high-energy-density batteries subjected to extreme conditions, such as intense charge/discharge cycles. The multi-layer model offers precise representations of heat dissipation and thermal gradients, which are critical for ensuring battery safety and durability in high-performance applications. Additionally, it facilitates the identification of localized failures or hotspots that simpler models may fail to detect. As previously mentioned, a 26650 cell consists of 38 layers, each comprising 8 components. To accurately capture the behavior of the entire multi-layer system, the multi-layer model involves a total of 306 equations. This is calculated as follows: 304 equations represent the 8 components (electrodes, separators, and collectors) across 38 layers, along with one additional equation for the electrolyte and another for the cell casing. The resulting state vector is denoted by $\mathbf{T}_{\text{multi}}(t) \in \mathbb{R}^{306\times 1}$. Note that in the electrolyte equation, the intermediate states are repetitive because the electrolyte is in contact with each component in every layer. Together, these equations offer a comprehensive representation of the system, defined as follows:

$$\dot{\mathbf{T}}_{\text{multi}}(t) = \mathcal{A}_{\text{multi}}\mathbf{T}_{\text{multi}}(t) + \mathcal{B}_{\text{multi}}\mathbf{u}(t), \tag{12}$$

$$\boldsymbol{y}_{\text{multi}}(t) = C_{\text{multi}}\mathbf{T}_{\text{multi}}(t), \tag{13}$$

where the input vector $\mathbf{u}(t)$ is given by:

$$\mathbf{u}(t) = \begin{bmatrix} T_{\text{air}}(t) & S(t) \end{bmatrix}^{\text{tr}} \in \mathbb{R}^{2\times 1}. \tag{14}$$

Here, $T_{\text{air}}(t)$ represents the air temperature, which is used as an input to show how external thermal conditions influence the model. Similarly, $S(t)$ denotes the electrochemical heat generated by reactions occurring inside the battery.

The matrices $\mathcal{A}_{\text{multi}}$, $\mathbf{T}_{\text{multi}}$, $\mathcal{B}_{\text{multi}}$, and C_{multi} are given by:

$$\mathcal{A}_{\text{multi}} = \begin{bmatrix} \mathcal{A}_{\text{single}}(1,1:9) & \left[\left[\mathcal{A}_{\text{single}}(1,2:9)\ldots\mathcal{A}_{\text{single}}(1,2:9)\right]_{37\ \text{times}}\ 0\right] \\ \mathcal{A}_{\text{single}}(2:9,:) & \mathbf{0}_{8\times 296} \\ \mathbf{0}_{296\times 296} & \begin{bmatrix} \mathcal{A}_{\text{single}}(2:9,:) \\ \vdots \\ \mathcal{A}_{\text{single}}(2:9,:) \end{bmatrix}_{37\ \text{times}} \\ \mathbf{0}_{1\times 296} & \mathcal{A}_{\text{single}}(10,:) \end{bmatrix} \in \mathbb{R}^{306\times 306}, \tag{15}$$

$$\mathcal{B}_{\text{multi}} = \begin{bmatrix} \mathcal{B}_{\text{single}}(1,:) \\ \begin{bmatrix} \mathcal{B}_{\text{single}}(2:9,:) \\ \vdots \\ \mathcal{B}_{\text{single}}(2:9,:) \end{bmatrix}_{304\ \text{times}} \\ \mathcal{B}_{\text{single}}(10,:) \end{bmatrix} \in \mathbb{R}^{306\times 2}, \tag{16}$$

$$C_{\text{multi}} = \begin{bmatrix} \mathbf{0}_{1\times 296} & C_{\text{single}} \end{bmatrix} \in \mathbb{R}^{1\times 306}. \tag{17}$$

The matrices $\mathcal{A}_{\text{single}}$, $\mathcal{B}_{\text{single}}$, and C_{single} are constructed by considering a single layer, using (3), (5), and (7) for each component. Substituting these matrices into (15), (16), and (17) allows the model to be expanded to include all layers within the battery. The matrices

$\mathcal{A}_{\text{single}}$, $\mathcal{B}_{\text{single}}$, and $\mathcal{C}_{\text{single}}$ are defined as follows:

$$\mathcal{A}_{\text{single}} = \begin{bmatrix} \alpha_1 & -\alpha_2 & -\alpha_3 & -\alpha_3 & -\alpha_3 & -\alpha_3 & -\alpha_3 & -\alpha_3 & -\alpha_3 & 0 \\ -\beta_1 & \beta_2 & 0 & 0 & 0 & 0 & 0 & 0 & 0 & 0 \\ -\gamma_1 & \gamma_2 & \gamma_3 & 0 & 0 & 0 & 0 & 0 & 0 & 0 \\ -\delta_1 & 0 & \delta_2 & \delta_3 & 0 & 0 & 0 & 0 & 0 & 0 \\ -\epsilon_1 & 0 & 0 & \epsilon_2 & \epsilon_3 & 0 & 0 & 0 & 0 & 0 \\ -\zeta_1 & 0 & 0 & 0 & \zeta_2 & \zeta_3 & 0 & 0 & 0 & 0 \\ -\eta_1 & 0 & 0 & 0 & 0 & \eta_2 & \eta_3 & 0 & 0 & 0 \\ -\theta_1 & 0 & 0 & 0 & 0 & 0 & \theta_2 & \theta_3 & 0 & 0 \\ -\iota_1 & 0 & 0 & 0 & 0 & 0 & 0 & \iota_2 & \iota_3 & 0 \\ 0 & 0 & 0 & 0 & 0 & 0 & 0 & 0 & \kappa_1 & \kappa_2 \end{bmatrix} \in \mathbb{R}^{10\times 10}, \tag{18}$$

$$\mathcal{B}_{\text{single}} = \begin{bmatrix} 0 & 0 & 0 & 0 & 0 & 0 & 0 & 0 & 0 & \lambda_1 \\ \lambda_2 & \lambda_3 & \lambda_4 & \lambda_5 & \lambda_6 & \lambda_7 & \lambda_8 & \lambda_9 & \lambda_{10} & 0 \end{bmatrix}^{\text{tr}} \in \mathbb{R}^{10\times 2}, \tag{19}$$

$$\mathcal{C}_{\text{single}} = \begin{bmatrix} 0 & 0 & 0 & 0 & 0 & 0 & 0 & 0 & 0 & 1 \end{bmatrix} \in \mathbb{R}^{1\times 10}. \tag{20}$$

The parameters and their definitions are provided in Appendix.

2.3. Electrochemical thermal power $S(t)$

Thermal power in electrochemical systems is given by:

$$S(t) = V(t)|I(t)|, \tag{21}$$

where $V(t)$ represents the voltage obtained from the electrochemical model, and $I(t)$ is the current applied to the battery. The use of the absolute value, $|I(t)|$, ensures that the thermal power remains positive, as heat generation is always a positive quantity [40, Chapter 2, Section 2.1], regardless of whether the current corresponds to charging or discharging. This approach captures the heat generated during both processes and remains consistent with the electrochemical model for $V(t)$.

An alternative formula for calculating $S(t)$ is $I(t)^2R$, where R is the internal resistance. However, R varies with factors such as temperature and state of charge, making its real-time estimation, $R(t)$, more challenging. The $V(t)|I(t)|$ method indirectly accounts for the effects of resistance through voltage, simplifying the computation while still accurately representing Joule heating.

The voltage $V(t)$ is calculated as the difference in solid-phase potentials:

$$V(t) = \phi_s^+(t) - \phi_s^-(t), \tag{22}$$

where

$$\phi_s^\pm(t) = \eta^\pm(t) + U^\pm\left(c_{ss}^\pm(t)\right) + FR^\pm j^\pm(t). \tag{23}$$

Here, $\eta^\pm(t)$ denotes the overpotential, $U^\pm(c_{ss}^\pm(t))$ the equilibrium potential, F the Faraday constant, and $R^\pm$ the internal resistance.

The reaction overpotential $\eta^\pm$ is given by:

$$\eta^\pm(t) = \frac{R_g T}{\alpha F} \sinh^{-1}\left(\frac{F}{2i_0^\pm(t)} j^\pm(t)\right), \tag{24}$$

where R_g is the gas constant, T the temperature, α the transfer coefficient, and $i_0^\pm$ the exchange current density:

$$i_0^\pm(t) = k^\pm\left[c_{ss}^\pm(t)\right]^{\alpha_c}\left[c_{e,0}\left(c_s^{\pm,\max} - c_{ss}^\pm(t)\right)\right]^{\alpha_a}, \tag{25}$$

where k is the reaction rate, $c_{ss}^\pm(t) \triangleq c_s^\pm(t, R_s^\pm)$ is the surface concentration, and $c_{e,0}$ the equilibrium electrolyte concentration.

The Single Particle Model (SPM) is employed for concentration dynamics, simplifying the electrodes to collections of spherical particles and focusing on lithium-ion diffusion in the solid phase while omitting electrolyte gradients. This model is computationally efficient, suitable for real-time battery management [41]. Fick's Law of Diffusion governs lithium transport within these particles, capturing radial migration between particle surfaces and cores. Fig. 2 illustrates the SPM structure with current collectors and radial lithium diffusion.

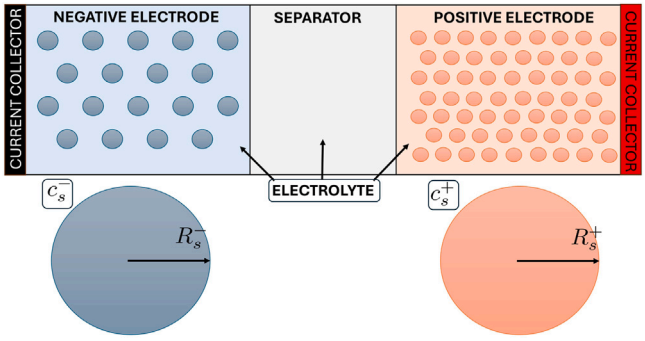

Fig. 2. SPM model.

The lithium concentrations in the electrodes follow:

$$\frac{\partial c_s^\pm}{\partial t}(t, r_s) = \frac{1}{r_s^2}\frac{\partial}{\partial r_s}\left[D_s^\pm r_s^2 \frac{\partial c_s^\pm}{\partial r_s}(t, r_s)\right], \tag{26}$$

$$t > 0, \quad r_s \in (0, R_s^\pm),$$

$$\frac{\partial c_s^\pm}{\partial r_s}(t, 0) = 0, \quad t > 0, \tag{27}$$

$$\frac{\partial c_s^\pm}{\partial r_s}(t, R_s^\pm) = -\frac{1}{D_s^\pm} j^\pm(t), \quad t > 0, \tag{28}$$

$$c_s^\pm(0, r_s) = c_{s,0}^\pm(r_s), \quad r_s \in [0, R_s^\pm], \tag{29}$$

where t and r_s are time and radial position. Here, $c_s^\pm$ denotes the solid-phase concentration, $D_s^\pm$ is the diffusion coefficient, and $j^\pm$ is the molar flux:

$$j^+(t) = -\frac{I(t)}{a_s^+ F L^+}, \quad j^-(t) = \frac{I(t)}{a_s^- F L^-}, \tag{30}$$

where $I(t)$ is current, $a_s^\pm$ is interfacial surface area, F the Faraday constant, and $L^\pm$ the electrode length.

The electrochemical model in this study employs the SPM to approximate lithium-ion transport and reaction kinetics within each electrode. While computationally efficient, the SPM inherently assumes uniform lithium concentration across electrode particles, neglecting electrolyte variations and potential non-uniform reaction distributions at high C-rates [42].

In the thermal model, heat generation is computed using the electrochemical reaction overpotentials, but the SPM does not resolve spatial variations within the electrodes. Consequently, in this framework, heat generation is assumed to be uniformly distributed across each electrode layer, with only radial heat conduction explicitly modeled. At high C-rates, significant local heat generation can occur within the positive electrode, potentially introducing axial (z-direction) temperature gradients that are not fully captured in a 2D model [43]. This effect may lead to localized overheating, which a Doyle–Fuller–Newman (DFN) model capable of resolving spatial variations in lithium concentration and temperature would be required to capture. However, for moderate C-rates, the dominant heat transfer path remains radial, making the 2D approach a reasonable compromise between accuracy and computational efficiency.

3. Temperature estimation

Due to the complexity of the multi-layer model, a simplified single-layer model was developed by considering only the first layer, which consists of 8 components within the battery, the electrolyte, and case. The temperature vector is denoted as $\mathbf{T}_{\text{single}(t)} \in \mathbb{R}^{10\times 1}$. The single-layer model, originally introduced in [30], simplifies the thermal dynamics of the battery components, enabling efficient real-time temperature

evaluation. Additionally, because designing an observer for the multi-layer model with 306 states is impractical, a Luenberger observer was applied to the single-layer model, as described in [30]. The single-layer model is redefined as:

$$\dot{\mathbf{T}}_{\text{single}}(t) = \mathcal{A}_{\text{single}}\mathbf{T}_{\text{single}}(t) + \mathcal{B}_{\text{single}}\mathbf{u}(t), \tag{31}$$

$$\boldsymbol{y}_{\text{single}}(t) = C_{\text{single}}\mathbf{T}_{\text{single}}(t). \tag{32}$$

In [30], the observer was developed for the single-layer model, considering two sensors. While the single-layer model presented here is designed with only one sensor, previous results using two theoretical sensors were utilized to explore observability configurations. A MATLAB code was developed to evaluate all possible configurations for sensor placement on the battery and to assess the system's potential observability. Specifically, the placement of two theoretical sensors on the battery was tested.

With 2 sensors and 10 possible locations for each, there are a total of $C_{10}^2 = 45$ combinations of C matrices, each having dimensions 2×10. However, after analyzing the observability Gramian for these configurations, only 6 were determined to be observable. In the configuration where sensors are placed in the negative electrode and outside the case, the significant difficulty of installing sensors within the negative electrode led to this configuration being excluded. This setup is represented mathematically as follows:

$$C([3;10]) = \begin{bmatrix} 0 & 0 & 1 & 0 & 0 & 0 & 0 & 0 & 0 & 0 \\ 0 & 0 & 0 & 0 & 0 & 0 & 0 & 0 & 0 & 1 \end{bmatrix} \tag{33}$$

Configurations where sensors are located in the separator and outside the case were also excluded due to the complexity of placing sensors within the separator. These configurations are represented as follows:

$$C([2;10]) = \begin{bmatrix} 0 & 1 & 0 & 0 & 0 & 0 & 0 & 0 & 0 & 0 \\ 0 & 0 & 0 & 0 & 0 & 0 & 0 & 0 & 0 & 1 \end{bmatrix}, \tag{34}$$

$$C([6;10]) = \begin{bmatrix} 0 & 0 & 0 & 0 & 0 & 1 & 0 & 0 & 0 & 0 \\ 0 & 0 & 0 & 0 & 0 & 0 & 0 & 0 & 0 & 1 \end{bmatrix}. \tag{35}$$

Similarly, configurations involving sensors placed in the positive electrode and outside the case were excluded due to installation difficulties. These configurations are described as:

$$C([7;10]) = \begin{bmatrix} 0 & 0 & 0 & 0 & 0 & 0 & 1 & 0 & 0 & 0 \\ 0 & 0 & 0 & 0 & 0 & 0 & 0 & 0 & 0 & 1 \end{bmatrix}, \tag{36}$$

$$C([9;10]) = \begin{bmatrix} 0 & 0 & 0 & 0 & 0 & 0 & 0 & 0 & 1 & 0 \\ 0 & 0 & 0 & 0 & 0 & 0 & 0 & 0 & 0 & 1 \end{bmatrix}. \tag{37}$$

In contrast, positioning the sensors outside on the positive collector tab and the case. This arrangement is both practical and feasible, as it simplifies the installation process. The corresponding configuration is given by:

$$C([8;10]) = \begin{bmatrix} 0 & 0 & 0 & 0 & 0 & 0 & 0 & 1 & 0 & 0 \\ 0 & 0 & 0 & 0 & 0 & 0 & 0 & 0 & 0 & 1 \end{bmatrix}. \tag{38}$$

The sensor placement should align with the radius used in the thermal resistance calculation. For instance, it can be positioned in the first layer, where the winding radius is minimal. Alternatively, the sensor can be applied to an intermediate layer corresponding to the average or maximum radius of the battery. In practical terms, the exact radius becomes less critical due to the significant challenges involved in placing a sensor inside the battery. This flexibility enables a more practical implementation while maintaining the overall effectiveness of the measurement.

The Luenberger observer estimates internal states using available measurements, defined by [44]:

$$\dot{\hat{\mathbf{T}}}_{\text{single}}(t) = \mathcal{A}_{\text{single}}\hat{\mathbf{T}}_{\text{single}}(t) + \mathcal{B}_{\text{single}}\mathbf{u}(t) + L[\boldsymbol{y}_{\text{single}} - C_{\text{single}}\hat{\mathbf{T}}_{\text{single}}(t)], \tag{39}$$

where $\mathcal{A}_{\text{single}}$, $\mathcal{B}_{\text{single}}$, and C_{single} are model parameters, and L is the observer gain. Defining the error $\tilde{\mathbf{T}}_{\text{single}}(t) = \mathbf{T}_{\text{single}}(t) - \hat{\mathbf{T}}_{\text{single}}(t)$, the error dynamics are given by:

$$\dot{\tilde{\mathbf{T}}}_{\text{single}}(t) = (\mathcal{A}_{\text{single}} - LC_{\text{single}})\tilde{\mathbf{T}}_{\text{single}}(t). \tag{40}$$

Theorem 1. *Choose the gain matrix $L \in \mathbb{R}^{10\times 2}$ such that $\mathcal{A}_{single} - LC_{single}$ is Hurwitz. For any initial states $\mathbf{T}_{single}(0)$ and $\hat{\mathbf{T}}_{single}(0)$, and any input $\mathbf{u}(t)$, the error $\tilde{\mathbf{T}}_{single}(t)$ converges exponentially to zero:*

$$\|\tilde{T}_{single}(t)\| \leq \|\tilde{T}_{single}(0)\| e^{-\frac{\lambda_{\min}(Q)}{2\lambda_{\max}(P)}t} \sqrt{\frac{\lambda_{\max}(P)}{\lambda_{\min}(P)}}. \tag{41}$$

Proof. Let the Lyapunov function be:

$$V(\tilde{\mathbf{T}}_{\text{single}}(t)) = \tilde{\mathbf{T}}_{\text{single}}(t)^{\text{tr}} P \tilde{\mathbf{T}}_{\text{single}}(t), \tag{42}$$

where P satisfies:

$$(\mathcal{A}_{\text{single}} - LC_{\text{single}})^{\text{tr}} P + P(\mathcal{A}_{\text{single}} - LC_{\text{single}}) = -Q, \tag{43}$$

with Q positive definite. By the Lyapunov theorem, P is positive definite.

From (42):

$$\lambda_{\min}(P)\|\tilde{T}_{\text{single}}(t)\|_2^2 \leq V(\tilde{T}_{\text{single}}(t)) \leq \lambda_{\max}(P)\|\tilde{T}_{\text{single}}(t)\|_2^2. \tag{44}$$

The derivative of $V(\tilde{\mathbf{T}}_{\text{single}}(t))$ is:

$$\dot{V}(\tilde{\mathbf{T}}_{\text{single}}(t)) = \dot{\tilde{\mathbf{T}}}_{\text{single}}(t)^{\text{tr}} P \tilde{\mathbf{T}}_{\text{single}}(t) + \tilde{\mathbf{T}}_{\text{single}}(t)^{\text{tr}} P \dot{\tilde{\mathbf{T}}}_{\text{single}}(t). \tag{45}$$

Substituting (40) and using (44), we obtain:

$$\begin{aligned} \dot{V}(\tilde{\mathbf{T}}_{\text{single}}(t)) &= -\tilde{\mathbf{T}}_{\text{single}}(t)^{\text{tr}} Q \tilde{\mathbf{T}}_{\text{single}}(t) \leq -\lambda_{\min}(Q)\|\tilde{\mathbf{T}}_{\text{single}}(t)\|_2^2 \\ &\leq \frac{-\lambda_{\min}(Q)}{\lambda_{\max}(P)} V(\tilde{\mathbf{T}}_{\text{single}}(t)). \end{aligned} \tag{46}$$

Applying the comparison principle gives:

$$V(\tilde{\mathbf{T}}_{\text{single}}(t)) \leq V(\tilde{\mathbf{T}}_{\text{single}}(0)) e^{-\frac{\lambda_{\min}(Q)}{\lambda_{\max}(P)}t}, \tag{47}$$

completing the proof. □

4. Model validation

Following the American Society of Mechanical Engineers (ASME) V&V 10 standards, this study validates the model's accuracy through a detailed comparison with experimental data obtained using NEWARE devices.

4.1. Experimental setup

Fig. 3 illustrates the experimental setup used to validate the thermal model with temperature data from charge and discharge cycles. A NEWARE BTS-4000 Series 5V12 A Battery Tester and an ESPEC Criterion Benchtop Chamber ensured precise control, with the BTS-4000 offering an accuracy of ±0.05% FS for current and voltage. To monitor potential temperature fluctuations during high-demand charge and discharge cycles, Type K thermocouples (accuracy ±1°C) were chosen for their wide temperature range and durability. These thermocouples were securely attached at three points (top, middle, bottom) along the battery's external surface using thermal tape to capture any temperature gradients, though results indicated a uniform surface temperature. Data were recorded at 1-second intervals using Neware BTS 8.0 software for current, voltage, and temperature, and subsequently compared to model simulations. The test battery, an ANR26650M1B cell from Lithium Werks, was charged at 10 A to 3.6 V and discharged to 2 V, with a 1 min rest between cycles to stabilize internal conditions. Tests were conducted at room temperature (21 °C) to simulate high-

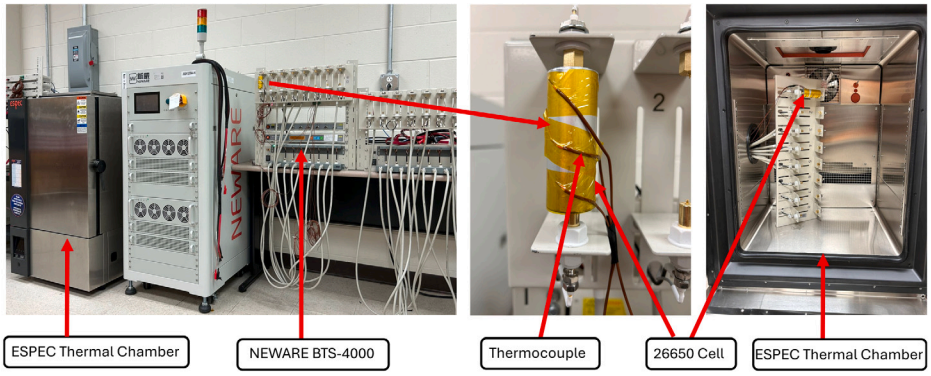

Fig. 3. Experimental setup.

Table 2
Parameters Used in the Simulation.

Category	Parameter	Value/Unit
Thermal Parameters	Density of Electrolyte (ρ_0)	1130 kg/m^3
	Density of Negative Collector (ρ_3)	8900 kg/m^3
	Density of Negative Electrode ($\rho_{2,4}$)	2500 kg/m^3
	Density of Positive Collector (ρ_7)	2700 kg/m^3
	Density of Positive Electrode ($\rho_{6,8}$)	1500 kg/m^3
	Density of Separator ($\rho_{1,5}$)	1200 kg/m^3
	Case Diameter (D_e)	25.85×10^{-3} m
	Initial Layer Diameter (D_i)	1.3×10^{-3} m
	Specific Heat Capacity of Case (c_9)	2420 J/(kg ·K)
	Specific Heat Capacity of Electrolyte (c_0)	2055.1 J/(kg ·K)
	Specific Heat Capacity of Negative Collector (c_3)	3440 J/(kg ·K)
	Specific Heat Capacity of Negative Electrode ($c_{2,4}$)	800 J/(kg ·K)
	Specific Heat Capacity of Positive Collector (c_7)	2420 J/(kg ·K)
	Specific Heat Capacity of Positive Electrode ($c_{6,8}$)	800 J/(kg ·K)
	Specific Heat Capacity of Separator ($c_{1,5}$)	800 J/(kg ·K)
	Thermal Conductivity of Negative Collector (K_3)	398 W/(m ·K)
	Thermal Conductivity of Negative Electrode ($K_{2,4}$)	1.04 W/(m ·K)
	Thermal Conductivity of Positive Collector ($K_{6,8}$)	238 W/(m ·K)
	Thermal Conductivity of Separator ($K_{1,5}$)	1 W/(m ·K)
	Thermal Resistance (R_1, Single Layer)	0.1715 K/W
	Thermal Resistance (R_1, Multilayer)	0.0071 K/W
	Thermal Resistance (R_2, Single Layer)	0.2634 K/W
	Thermal Resistance (R_2, Multilayer)	0.0126 K/W
	Thermal Resistance (R_3, Single Layer)	0.2515 K/W
	Thermal Resistance (R_3, Multilayer)	0.0162 K/W
	Thermal Resistance (R_6, Single Layer)	4.3684×10^{-4} K/W
	Thermal Resistance (R_6, Multilayer)	3.1187×10^{-5} K/W
	Thermal Resistance (R_7, Single Layer)	4.3684×10^{-4} K/W
	Thermal Resistance (R_7, Multilayer)	3.1187×10^{-5} K/W

(*continued on next page*)

demand conditions, such as those encountered in electric vehicles, over 100 cycles.

4.2. Validation of single-layer and multi-layer models using experimental results

The simulations were performed using MATLAB on an MSI PC equipped with an Intel i7-13620H CPU, 16 GB of RAM, and an NVIDIA GeForce RTX 4050 GPU with 6 GB of memory. The thermal and electrochemical parameters used in the simulation were obtained from [45] and are shown in Table 2. The convective heat transfer coefficient of the electrolyte used in the simulations was set to 9.5 W/(m^2 · K).

In the single-layer model, the electrolyte volume was normalized to emphasize its relative impact on thermal behavior within an individual layer. The normalization of physical parameters, such as volume, is a well-established methodology in thermal modeling. Following [46], this study normalizes the electrolyte volume to highlight its contribution to thermal behavior, ensuring consistent and scalable results in the single-layer model. This normalization facilitates direct comparison of the electrolyte's thermal influence with other components

Table 2 (*continued*).

Category	Parameter	Value/Unit
Geometric Parameters	Electrolyte Volume (Single-layer)	0.9109 (normalized)
	Electrolyte Volume (Multi-layer)	3.0894×10^{-5} m^3
	Components Volume (Single-layer and Multi-layer)	3.0894×10^{-5} m^3
Electrochemical Parameters	Faraday Constant (F)	96487 C/mol
	Gas Constant (R)	8.314 J/(mol ·K)
	Height (H)	65.15×10^{-3} m
	Negative Electrode Diffusion Coefficient (D_n)	3.0×10^{-14} m^2/s
	Negative Electrode Radius (R_n)	3.65×10^{-8} m
	Porosity of Negative Electrode (ϵ_n)	0.54
	Positive Electrode Diffusion Coefficient (D_p)	2.5×10^{-16} m^2/s
	Positive Electrode Radius (R_p)	3.5×10^{-6} m
	Thickness of Negative Collector (L_3)	1×10^{-5} m
	Thickness of Negative Electrode ($L_{2,4}$)	3.5×10^{-5} m
	Thickness of Positive Collector (L_7)	2×10^{-5} m
	Thickness of Separator ($L_{1,5}$)	2×10^{-5} m

and ensures dimensional consistency in the application of the heat equation. Thermal resistances in this model were calculated using the smallest radius inside the battery ($r_1 = 1.1$ mm), which reflects the local effects near the battery core for precise layer-level analysis. Conversely, the multi-layer model employs absolute volumes of all components, naturally representing their cumulative thermal contributions without requiring normalization. The total system volume inherently integrates the relative effects of the electrolyte and other components across the layers. The thermal resistance R_i for each component ($i \in \overline{1,9}$) was calculated as follows: In the single-layer model, r_1 is 1.1 mm (corresponding to the battery center), while r_2 represents this radius plus the combined thicknesses of all components. For the multi-layer model, r_1 is set to the average radius of the battery to simplify calculations. Preliminary analysis revealed minimal variation in thermal resistance between layers, supporting the use of an average thermal resistance across the system. The normalization of the electrolyte volume in the single layer is given by:

$$v_{0,\text{single}} = \frac{v_0}{v_{\text{total}}}, \tag{48}$$

where v_0 is the electrolyte volume used in the multi-layer model, and v_{total} is the total volume of the battery.

For consistency, the effective heat generation in the electrolyte in the single-layer is defined as:

$$Q_{0,\text{eff}}(t) = \frac{Q_0(t)}{v_{0,\text{single}}}, \tag{49}$$

where $Q_0(t)$ is the heat generation rate in the electrolyte, expressed in $\frac{\text{W}}{\text{m}^3}$, and $v_{0,\text{single}}$ is the normalized volume of the electrolyte. This ensures dimensional consistency when applying the normalization approach.

The equilibrium potentials $U^{\pm}(c_{ss}^{\pm}(t))$ for voltage $V(t)$ are:

$$\begin{aligned} U^{+}(c_{ss}^{+}(t)) &= 8.3538 - 1.1743 \exp\left(-80.2493(1 - c_{ss}^{+}(t))^{1.3198}\right) \\ &- 7.8962 \times 10^{-6} \exp\left(20.2645(1 - c_{ss}^{+}(t))^{3.8003}\right) \\ &+ 7.8986 \times 10^{-6} \exp\left(20.2645(1 - c_{ss}^{+}(t))^{3.7995}\right), \end{aligned} \tag{50}$$

$$\begin{aligned} U^{-}(c_{ss}^{-}(t)) &= 5.3679 + 0.5416 \exp\left(-305.5309 c_{ss}^{-}(t)\right) \\ &+ 0.044 \tanh\left(\frac{\theta^{-} c_{ss}^{-}(t) - 0.1958}{0.1088}\right) - 0.1978 \tanh\left(\frac{c_{ss}^{-}(t) - 1.0571}{0.0854}\right) \\ &- 0.687 \tanh\left(\frac{c_{ss}^{-}(t) - 0.0117}{0.0529}\right) - 0.0175 \tanh\left(\frac{c_{ss}^{-}(t) - 0.5692}{0.0875}\right), \end{aligned} \tag{51}$$

The equilibrium potential equations were adapted from [45], with parameter identification performed in MATLAB. The coefficients were optimized through an iterative fitting procedure to minimize the Root Mean Square Error (RMSE) between the simulated and experimental voltage curves.

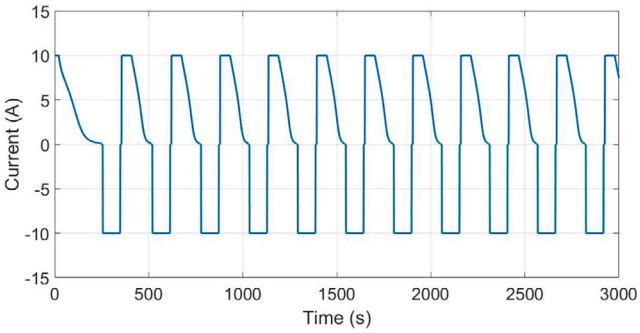

(a) Current Profile.

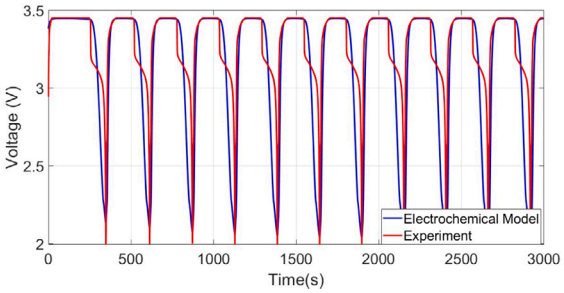

(b) Comparison of SPM model and experimental voltage data.

Fig. 4. (a) Current profile used in the model. (b) Comparison of SPM model and experimental voltage data.

The simulation spans 2.5×10^4 seconds; however, only the first 5000 s are shown for clarity. Fig. 4(a) shows the current profile used in the tests, cycling between 10 A and −10 A over 100 cycles. Fig. 4(b) compares the voltage response from the SPM model (blue) with experimental data (red). The model captures the periodic voltage oscillations during charge/discharge cycles well, matching the amplitude and frequency of the experimental data. Minor discrepancies at peak voltages suggest areas for further refinement, such as accounting for unmodeled electrochemical effects.

Fig. 5 presents a comparison between the multi-layer model, single-layer model, and experimental temperature data to validate the thermal model. While both models perform adequately, the single-layer model

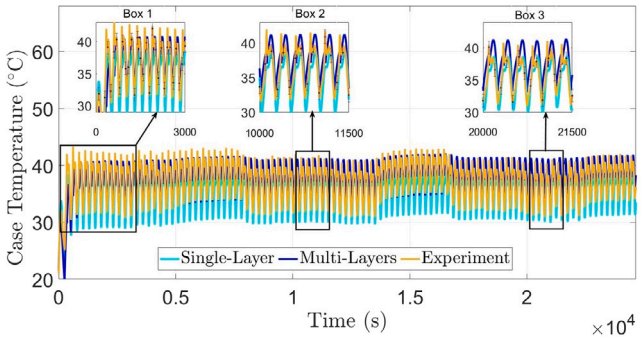

Fig. 5. Single-layer vs multi-layer vs experiments results.

(cyan) exhibits more pronounced deviations, particularly during temperature drops. In contrast, the multi-layer model (blue) closely aligns with the experimental data (yellow), offering a more detailed representation of internal heat distribution. The three zoomed-in regions highlight these distinctions. In the first segment, around 3000 s, the multi-layer model accurately captures both the peaks and troughs observed in the experimental data, whereas the single-layer model underestimates these fluctuations. In the second zoomed section, between 10000 s and 11500 s, the single-layer model further underestimates the temperature valleys during cooling periods. Finally, in the third zoomed section, between 20000 s and 21500 s, the multi-layer model continues to align well with the experimental results, while the single-layer model underestimates the temperature variations.

To quantify the accuracy of the models, the RMSE was computed for both voltage Fig. 4(b) and case temperature Fig. 5 comparisons. The results show:

- **SPM Model (Voltage,** Fig. 4(b)): RMSE = 0.482 V
- **Multi-Layer Model (Thermal,** Fig. 5): RMSE = 1.99 °C
- **Single-Layer Model (Thermal,** Fig. 5): RMSE = 2.39 °C

These values confirm that the SPM model provides a reasonable match to experimental voltage data, while the multi-layer thermal model improves agreement with experimental temperature data, reducing RMSE by approximately 16.7% compared to the single-layer model. It is important to acknowledge that the experimental temperature measurements have an accuracy of ±1°C due to the Type K thermocouples used in this study. As a result, any discrepancies within this range may be influenced by sensor limitations rather than inherent model inaccuracies. However, as shown in Fig. 5, the observed differences between the multi-layer and single-layer models exceed ±1°C in most cases, indicating that the trends captured by the models are meaningful despite this uncertainty. Furthermore, while parameter variations (as outlined in Table 2) may introduce additional uncertainties, these parameters were derived systematically from literature sources and thermal resistance equations rather than arbitrary assumptions. Consequently, the comparison remains valid, particularly when evaluating the relative accuracy of the two modeling approaches.

In Fig. 6(a), the single-layer model shows a larger temperature difference, or ΔT, across battery components. This occurs due to the model's simplifications, which lead to an overestimation of temperature fluctuations. The single-layer model's simplified approach fails to capture the subtle, component-specific variations in heat distribution, resulting in a less accurate depiction of the battery's internal thermal dynamics. In contrast, Fig. 6(b), representing the multi-layer model, demonstrates a more accurate and detailed simulation of temperatures across the battery's layers. The average temperature of each component $i \in \overline{1,8}$, is computed by aggregating its 38 associated temperature states across the layers of the battery: $\bar{T}_i(t) = \frac{1}{38}\sum k = 1^{38} T_{38(k-1)+i}(t)$. Further, the two separators, two negative electrodes, and two positive electrodes are averaged pairwise as follows: $\bar{T}_{1,5}(t) = \frac{1}{2}\left(\bar{T}_1(t) + \bar{T}_5(t)\right)$,

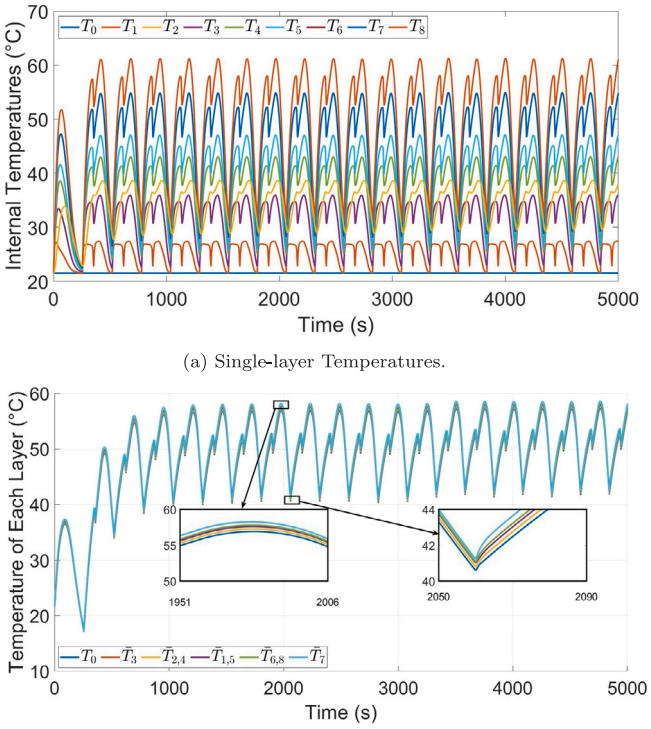

(a) Single-layer Temperatures.

(b) Internal temperatures in multi-layer.

Fig. 6. Comparison internal temperatures single-layer and multi-layer.

$\bar{T}_{2,4}(t) = \frac{1}{2}\left(\bar{T}_2(t) + \bar{T}_4(t)\right)$, and $\bar{T}_{6,8}(t) = \frac{1}{2}\left(\bar{T}_6(t) + \bar{T}_8(t)\right)$. This results in six final internal temperatures used for visualization and analysis: electrolyte, separator, negative electrode, positive electrode, negative collector, and positive collector. By modeling each layer individually, the multi-layer model better reflects the true thermal behavior of the battery, producing smaller, more realistic ΔT values. This approach aligns more closely with actual thermal gradients within the battery, illustrating how different components reach distinct temperatures during charge and discharge cycles. This accuracy is essential for effective thermal management, as it helps identify and mitigate localized hotspots, ultimately enhancing the battery's performance and safety.

For safety and practical reasons, this study restricts thermocouple placement to the battery case, as inserting them directly into the battery poses a risk of triggering thermal runaway. Nonetheless, some research has explored internal thermocouple placement to achieve more accurate temperature measurements despite associated safety challenges. For instance, [47] developed a technique for embedding thermocouples within cylindrical cells and observed that internal temperatures could significantly exceed surface readings, particularly under dynamic loading conditions. Similarly, [48] placed thermocouples radially within the jelly-roll structure to examine temperature gradients, revealing substantial differences due to limited internal heat conduction. Protective coatings were applied to the thermocouple tips to prevent chemical interactions and structural damage. In another study, [49] reported temperature variations of up to 10 °C between the core and surface of $LiFePO_4$ cells, emphasizing the importance of internal measurements for capturing accurate thermal behavior. These studies demonstrate the value of internal thermocouples in providing detailed thermal data, although their use involves risks such as short circuits and structural integrity issues. Consequently, well-designed models and non-invasive monitoring methods are crucial for safely estimating internal temperatures. The internal temperature trends shown in Fig. 6(b) are consistent with findings from [47,49]. Both studies highlight that internal temperatures are notably higher than surface measurements, with [49] documenting differences exceeding 10 °C. Our

multi-layer model results similarly indicate a temperature difference of approximately 15 °C between internal and surface measurements, further validating its accuracy in capturing essential internal thermal dynamics.

Fig. 7(a) illustrates the estimation error between the thermal model and the Luenberger observer, where the model's initial temperature is set to 25 °C, while the observer starts at 0 °C to intentionally introduce a discrepancy for performance evaluation. Despite this initial difference, the observer's estimates converge rapidly toward the actual thermal states of the single-layer model. The close agreement between the measured T_9 and the estimated $\hat{T}_9$ validates the accuracy of the observer design. Fig. 7(b) shows the error dynamics of the system's thermal states, with each line representing the error of a specific temperature. Initially, the errors are large due to the differing initial conditions but steadily diminish, demonstrating the observer's ability to effectively track the temperature states. Fig. 7(c) illustrates the 2-Norm of the observer error over time, representing the overall estimation error across all system components. The norm begins at a high initial value but decreases rapidly, stabilizing close to zero within approximately 400 s. This behavior underscores the efficiency and reliability of the observer in minimizing errors, making it suitable for real-time applications requiring precise temperature estimation. These results collectively demonstrate the Luenberger observer's effectiveness and robustness in capturing the thermal dynamics of the system under dynamic conditions.

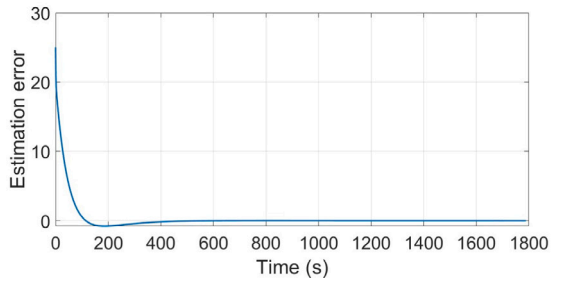

(a) Estimation error for the case temperature (T_9).

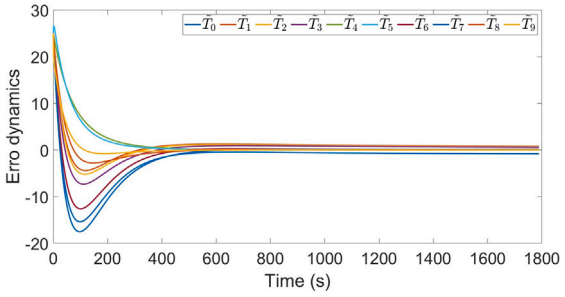

(b) Error dynamics for individual temperature.

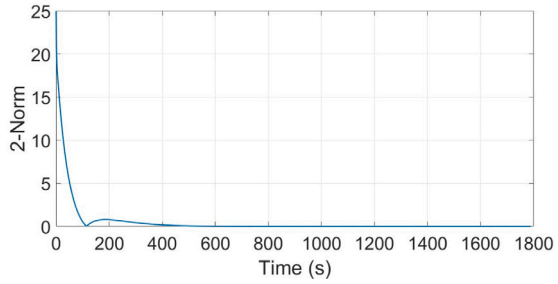

(c) 2-Norm.

Fig. 7. Estimation performance of the Luenberger observer for the thermal model: (a) Estimation error for the case temperature, comparing measured and estimated values. (b) Error dynamics for individual temperature, showing the convergence of the observer. (c) 2-Norm of the observer error over time, representing the overall estimation accuracy across all states.

4.3. Comparison between multi-layer and single-layer models

The multi-layer model provides a high-fidelity representation of internal temperature distributions by explicitly modeling each of the 38 layers within the LiB in a total of 306 coupled equations. This model captures localized thermal gradients, heat dissipation paths, and electrochemical interactions, making it particularly suitable for applications requiring precise temperature estimation, such as hotspot detection and failure analysis. However, the computational complexity of the multi-layer model poses challenges for real-time applications. Battery management systems, real-time control, and onboard diagnostics require fast and computationally efficient models, making the direct implementation of the multi-layer approach impractical in embedded systems. To address this, the single-layer model simplifies the multi-layer approach by aggregating all layers into a single representative layer, significantly reducing computational costs while maintaining reasonable accuracy for estimating the case temperature. This model accounts for variations in component volume and thermal resistance to preserve dimensional consistency, enabling a fair comparison with the multi-layer model. While the single-layer model sacrifices some internal temperature resolution, its reduced complexity allows for practical implementation in real-time applications, including temperature monitoring and sensor placement optimization. Notably, this model is also utilized in the Luenberger observer design, where a multi-layer observer would be computationally prohibitive.

The choice between these models depends on the intended application:

- The multi-layer model is advantageous for detailed thermal analysis, hotspot detection, and battery cooling strategy optimization.
- The single-layer model is better suited for real-time applications, computationally efficient estimation, and battery monitoring systems.

5. Conclusion

This study highlights the critical role of advanced modeling techniques in improving the accuracy and reliability of battery thermal and electrochemical analysis. The multi-layer model demonstrated its ability to capture detailed internal thermal dynamics, accurately representing temperature gradients across battery components. This fidelity is particularly valuable for optimizing battery performance, safety, and longevity in applications with demanding thermal conditions, such as electric vehicles and grid storage systems. While the single-layer model enables computational efficiency and reasonably estimates of case temperature, it has limitations in capturing internal thermal behaviors, resulting in discrepancies in key metrics such as temperature fluctuations and internal gradients. Nevertheless, its simplicity and scalability make it a practical tool for preliminary assessments and applications with limited computational resources. The multi-layer model's accurate reflection of internal thermal states positions it as a valuable resource for enhancing thermal management strategies. Furthermore, the Luenberger observer demonstrated robust performance in tracking thermal dynamics under dynamic conditions, with rapid convergence and minimal error. Its integration into BMS could provide real-time temperature estimation and early warnings for thermal anomalies, contributing to proactive safety measures.

Future research could focus on incorporating methods to account for uncertainties in material properties, manufacturing variations, and environmental factors, improving the robustness and reliability of the models under diverse operating conditions. The Doyle–Fuller–Newman (DFN) model, which resolves spatial variations in lithium concentration, will be applied to improve model accuracy and mitigate the

limitations of the SPM at high C-rates. Addressing these uncertainties would enhance accuracy and broaden the applicability of the models to various battery chemistries and configurations. In addition, the development of integrated fault detection frameworks within electrochemical-thermal models could help identify anomalies, such as sensor malfunctions or abnormal thermal behaviors, ensuring early warning systems for enhanced battery safety. Relaxing the adiabatic boundary condition would result in a PDE that accounts for spatial variables. Investigating the interactions between aging mechanisms and thermal dynamics would provide a more comprehensive understanding of long-term battery performance. Advanced internal sensing technologies or non-invasive monitoring methods could also be explored to further validate and refine the multi-layer model while maintaining safety during operation. These advancements would collectively contribute to the development of safer, more efficient, and longer-lasting battery systems.

CRediT authorship contribution statement

Patryck Ferreira: Writing – review & editing, Writing – original draft, Validation, Methodology, Investigation, Formal analysis, Data curation, Conceptualization. **Shu-Xia Tang:** Writing – review & editing, Supervision, Project administration, Methodology, Investigation, Formal analysis, Data curation, Conceptualization.

Declaration of competing interest

The authors declare that they have no known competing financial interests or personal relationships that could have appeared to influence the work reported in this paper.

Appendix. Parameter definitions

The following expressions provide the parameter definitions used in Section 2.2.2.

$$\alpha_1 = \frac{h(A+nA_1)}{\Psi_0}, \quad \alpha_2 = \frac{hA}{\Psi_0}, \quad \alpha_3 = \frac{hA_1}{\Psi_0},$$
$$\beta_1 = \frac{hAR_1+1}{\Psi_1 R_1}, \quad \beta_2 = \frac{hAR_1-1}{\Psi_1 R_1},$$
$$\gamma_1 = \frac{hA_1}{\Psi_2}, \quad \gamma_2 = \frac{1}{\Psi_2 R_2}, \quad \gamma_3 = \frac{hA_1R_2-1}{\Psi_2 R_2},$$
$$\delta_1 = \frac{hA_1}{\Psi_3}, \quad \delta_2 = \frac{1}{\Psi_3 R_3}, \quad \delta_3 = \frac{hA_1R_3-1}{\Psi_3 R_3},$$
$$\epsilon_1 = \frac{hA_1}{\Psi_4}, \quad \epsilon_2 = \frac{1}{\Psi_4 R_4}, \quad \epsilon_3 = \frac{hA_1R_4-1}{\Psi_4 R_4},$$
$$\zeta_1 = \frac{hA_1}{\Psi_5}, \quad \zeta_2 = \frac{1}{\Psi_5 R_5}, \quad \zeta_3 = \frac{hA_1R_5-1}{\Psi_5 R_5},$$
$$\eta_1 = \frac{hA_1}{\Psi_6}, \quad \eta_2 = \frac{1}{\Psi_6 R_6}, \quad \eta_3 = \frac{hA_1R_6-1}{\Psi_6 R_6},$$
$$\theta_1 = \frac{hA_1}{\Psi_7}, \quad \theta_2 = \frac{1}{\Psi_7 R_7}, \quad \theta_3 = \frac{hA_1R_7-1}{\Psi_7 R_7},$$
$$\iota_1 = \frac{hA_1}{\Psi_8}, \quad \iota_2 = \frac{1}{\Psi_8 R_8}, \quad \iota_3 = \frac{hA_1R_8-1}{\Psi_8 R_8},$$
$$\kappa_1 = \frac{1}{\Psi_9 R_9}, \quad \kappa_2 = \frac{-R_{\text{air}}-R_9}{\Psi_9 R_9 R_{\text{air}}}, \quad \lambda_1 = \frac{-1}{\mu_9 R_{\text{air}}},$$
$$\lambda_2 = \frac{1}{\mu_0}, \quad \lambda_3 = \frac{1}{\mu_1}, \quad \lambda_4 = \frac{1}{\mu_2},$$
$$\lambda_5 = \frac{1}{\mu_3}, \quad \lambda_6 = \frac{1}{\mu_4}, \quad \lambda_7 = \frac{1}{\mu_5},$$
$$\lambda_8 = \frac{1}{\mu_6}, \quad \lambda_9 = \frac{1}{\mu_7}, \quad \lambda_{10} = \frac{1}{\mu_8},$$

where n in α_1 represents the number of interactions between the electrolyte and each component within a layer, $\Psi_i = \rho_i c_{\text{p}i} v_i$ and $\mu_i = \rho_i c_{\text{p}i} v_j$ for $i \in \overline{0,9}$ and $j \in \overline{0,8}$.

Data availability

Data will be made available on request.

References

[1] A. Yoshino, The birth of the lithium-ion battery, Angew. Chem. Int. Ed. 51 (24) (2012) 5798–5800.
[2] B. Diouf, R. Pode, Potential of lithium-ion batteries in renewable energy, Renew. Energy 76 (2015) 375–380.
[3] P. Bernard, M. Lippert, Nickel–cadmium and nickel–metal hydride battery energy storage, in: Electrochemical Energy Storage for Renewable Sources and Grid Balancing, Elsevier, 2015, pp. 223–251.
[4] D. Deng, Li-ion batteries: basics, progress, and challenges, Energy Sci. Eng. 3 (5) (2015) 385–418.
[5] M. Malik, K.H. Chan, G. Azimi, Review on the synthesis of LiNixMnyCo1-x-yO2 (NMC) cathodes for lithium-ion batteries, Mater. Today Energy 28 (2022) 101066.
[6] A. Nekahi, A.K. MR, X. Li, S. Deng, K. Zaghib, Sustainable LiFePO4 and LiMnxFe1-xPO4 (x=0.1–1) cathode materials for lithium-ion batteries: A systematic review from mine to chassis, Mater. Sci. Eng.: R: Rep. 159 (2024) 100797.
[7] J. Arteaga, H. Zareipour, V. Thangadurai, Overview of lithium-ion grid-scale energy storage systems, Curr. Sustain./Renew. Energy Rep. 4 (2017) 197–208.
[8] Y. Zeng, D. Chalise, S.D. Lubner, S. Kaur, R.S. Prasher, A review of thermal physics and management inside lithium-ion batteries for high energy density and fast charging, Energy Storage Mater. 41 (2021) 264–288.
[9] P. Lyu, X. Liu, J. Qu, J. Zhao, Y. Huo, Z. Qu, Z. Rao, Recent advances of thermal safety of lithium ion battery for energy storage, Energy Storage Mater. 31 (2020) 195–220.
[10] Y. Yang, R. Wang, Z. Shen, Q. Yu, R. Xiong, W. Shen, Towards a safer lithium-ion batteries: A critical review on cause, characteristics, warning and disposal strategy for thermal runaway, Adv. Appl. Energy 11 (2023) 100146.
[11] X. Feng, M. Ouyang, X. Liu, L. Lu, Y. Xia, X. He, Thermal runaway mechanism of lithium ion battery for electric vehicles: A review, Energy Storage Mater. 10 (2018) 246–267.
[12] C. Park, A.K. Jaura, Dynamic Thermal Model of Li-Ion Battery for Predictive Behavior in Hybrid and Fuel Cell Vehicles, Tech. Rep., SAE Technical Paper, 2003.
[13] B. Csomós, S. Kocsis Szürke, D. Fodor, Comparison of coupled electrochemical and thermal modelling strategies of 18650 Li-Ion batteries in finite element analysis—A review, Materials 16 (24) (2023) 7613.
[14] L. Saw, Y. Ye, A. Tay, Electrochemical–thermal analysis of 18650 Lithium Iron Phosphate cell, Energy Convers. Manage. 75 (2013) 162–174.
[15] M. Ghalkhani, F. Bahiraei, G.-A. Nazri, M. Saif, Electrochemical–thermal model of pouch-type lithium-ion batteries, Electrochim. Acta 247 (2017) 569–587.
[16] X. Zhang, P. Li, B. Huang, H. Zhang, Numerical investigation on the thermal behavior of cylindrical lithium-ion batteries based on the electrochemical-thermal coupling model, Int. J. Heat Mass Transfer 199 (2022) 123449.
[17] Z. Wang, J. Ma, L. Zhang, Finite element thermal model and simulation for a cylindrical Li-ion battery, IEEE Access 5 (2017) 15372–15379.
[18] Y. Li, Z. Zhou, W.-T. Wu, Three-dimensional thermal modeling of Li-ion battery cell and 50 V Li-ion battery pack cooled by mini-channel cold plate, Appl. Therm. Eng. 147 (2019) 829–840.
[19] K.E. Thomas, J. Newman, R.M. Darling, Mathematical modeling of lithium batteries, in: Advances in Lithium-Ion Batteries, Springer, 2002, pp. 345–392.
[20] X. Lin, H.E. Perez, J.B. Siegel, A.G. Stefanopoulou, Y. Li, R.D. Anderson, Y. Ding, M.P. Castanier, Online parameterization of lumped thermal dynamics in cylindrical lithium ion batteries for core temperature estimation and health monitoring, IEEE Trans. Control Syst. Technol. 21 (5) (2013) 1745–1755.
[21] F. He, A.A. Ams, Y. Roosien, W. Tao, B. Geist, K. Singh, Reduced-order thermal modeling of liquid-cooled lithium-ion battery pack for EVs and HEVs, in: 2017 IEEE Transportation Electrification Conference and Expo, ITEC, IEEE, 2017, pp. 507–511.
[22] C. Zhang, K. Li, J. Deng, Real-time estimation of battery internal temperature based on a simplified thermoelectric model, J. Power Sources 302 (2016) 146–154.
[23] J. Zhang, X.-G. Yang, F. Sun, Z. Wang, C.-Y. Wang, An online heat generation estimation method for lithium-ion batteries using dual-temperature measurements, Appl. Energy 272 (2020) 115262.
[24] R.R. Richardson, S. Zhao, D.A. Howey, On-board monitoring of 2-D spatially-resolved temperatures in cylindrical lithium-ion batteries: Part II. State estimation via impedance-based temperature sensing, J. Power Sources 327 (2016) 726–735.
[25] X. Liu, Y. Li, Y. Kang, G. Zhao, B. Duan, C. Zhang, An accurate co-estimation of core temperature and state of charge for lithium-ion batteries with electrothermal model, IEEE J. Emerg. Sel. Top. Power Electron. 12 (1) (2023) 231–241.

[26] X. Lin, A.G. Stefanopoulou, H.E. Perez, J.B. Siegel, Y. Li, R.D. Anderson, Quadruple adaptive observer of the core temperature in cylindrical Li-ion batteries and their health monitoring, in: 2012 American Control Conference, ACC, IEEE, 2012, pp. 578–583.
[27] X. Lin, H.E. Perez, J.B. Siegel, A.G. Stefanopoulou, Y. Li, R.D. Anderson, Y. Ding, M.P. Castanier, Online parameterization of lumped thermal dynamics in cylindrical lithium-ion batteries for core temperature estimation and health monitoring, IEEE Trans. Control Syst. Technol. 21 (5) (2012) 1745–1755.
[28] M.S. Rad, D.L. Danilov, M. Baghalha, M. Kazemeini, P.H. Notten, Thermal modeling of cylindrical $LiFePO_4$ batteries, J. Mod. Phys. 4 (2013) 1–7.
[29] P. Ferreira, S.-X. Tang, Advancement in lithium-ion battery pack thermal modeling based on electrochemical principles, in: Heat Transfer Summer Conference, Vol. 87905, American Society of Mechanical Engineers, 2024, V001T01A006.
[30] P. Ferreira, S.-X. Tang, Sensors placement analysis and temperature estimation in lithium-ion batteries with a cascaded electrochemical-thermal model, in: 2024 European Control Conference, ECC, IEEE, 2024, pp. 200–205.
[31] J. Wang, X. Guo, Z. Luo, H. Yang, M. Chen, K. Wang, A safety design strategy for practical lithium-ion pouch cells, Electrochim. Acta 465 (2023) 142992.
[32] W. Kao-ian, R. Pornprasertsuk, P. Thamyongkit, T. Maiyalagan, S. Kheawhom, Rechargeable zinc-ion battery based on choline chloride-urea deep eutectic solvent, J. Electrochem. Soc. 166 (6) (2019) A1063–A1069.
[33] H. Bhundiya, B. Hunt, B. Drolen, Measurement of the effective radial thermal conductivities of 18650 and 26650 lithium ion battery cells, in: Thermal and Fluid Analysis Workshop, NASA Jet Propulsion Laboratory, Galveston, 2018.
[34] N.T. Tran, T. Farrell, M. Vilathgamuwa, Y. Li, et al., A computationally efficient coupled electrochemical-thermal model for large format cylindrical lithium ion batteries, J. Electrochem. Soc. 166 (13) (2019) A3059.
[35] T.L. Bergman, A.S. Lavine, F.P. Incropera, D.P. DeWitt, Introduction to Heat Transfer, John Wiley & Sons, 2011.
[36] C.-W. Wu, X. Ren, W.-X. Zhou, G. Xie, G. Zhang, Thermal stability and thermal conductivity of solid electrolytes, APL Mater. 10 (4) (2022).
[37] S. Chen, C. Wan, Y. Wang, Thermal analysis of lithium-ion batteries, J. Power Sources 140 (1) (2005) 111–124.
[38] C. He, Q. Yue, M. Wu, Q. Chen, T. Zhao, A 3D electrochemical-thermal coupled model for electrochemical and thermal analysis of pouch-type lithium-ion batteries, Int. J. Heat Mass Transfer 181 (2021) 121855.
[39] D. Wang, H. Huang, Z. Tang, Q. Zhang, B. Yang, B. Zhang, A lithium-ion battery electrochemical–thermal model for a wide temperature range applications, Electrochim. Acta 362 (2020) 137118.
[40] C. Ya, A. Ghajar, H. Ma, Heat and Mass Transfer Fundamentals & Applications, McGraw- Hill, 2015.
[41] N.A. Chaturvedi, R. Klein, J. Christensen, J. Ahmed, A. Kojic, Algorithms for advanced battery-management systems, IEEE Control Syst. Mag. 30 (3) (2010) 49–68.
[42] J. Li, N. Lotfi, R.G. Landers, J. Park, A single particle model for lithium-ion batteries with electrolyte and stress-enhanced diffusion physics, J. Electrochem. Soc. 164 (4) (2017) A874.
[43] A. Saxon, C. Yang, S. Santhanagopalan, M. Keyser, A. Colclasure, Li-ion battery thermal characterization for thermal management design, Batteries 10 (4) (2024) 136.
[44] R.L. Williams, D.A. Lawrence, et al., Linear State-Space Control Systems, John Wiley & Sons, 2007.
[45] J. Chiew, C.S. Chin, W.D. Toh, Z. Gao, J. Jia, C.Z. Zhang, A pseudo three-dimensional electrochemical-thermal model of a cylindrical $LiFePO_4$-graphite battery, Appl. Therm. Eng. 147 (2019) 450–463.
[46] A. König-Haagen, S. Höhlein, A. Lázaro, M. Delgado, G. Diarce, D. Groulx, F. Herbinger, A. Patil, G. Englmair, G. Wang, et al., Analysis of the discharging process of latent heat thermal energy storage units by means of normalized power parameters, J. Energy Storage 72 (2023) 108428.
[47] B. Gulsoy, T. Vincent, J. Sansom, J. Marco, In-situ temperature monitoring of a lithium-ion battery using an embedded thermocouple for smart battery applications, J. Energy Storage 54 (2022) 105260.
[48] X. Yu, Q. Wu, R. Huang, X. Chen, A novel heat generation acquisition method of cylindrical battery based on core and surface temperature measurements, J. Electrochem. Energy Convers. Storage 19 (3) (2022) 030905.
[49] C. Forgez, D.V. Do, G. Friedrich, M. Morcrette, C. Delacourt, Thermal modeling of a cylindrical LiFePO4/graphite lithium-ion battery, J. Power Sources 195 (9) (2010) 2961–2968.